

NMR/NQR and AC-susceptibility Studies in the Weyl Semimetal Superconductor $1T\text{-MoTe}_2$ under Pressure

T. Fujii^{1,2}, H. Yasuoka¹, M. O. Ajeesh[†], M. Schmidt¹, T. Mito², Yu Liu^{3,†}, C. Petrovic^{3,*} and M. Baenitz¹

¹*Max Planck Institute for Chemical Physics of Solids, 01187 Dresden, Germany*

²*Graduate School of Science, University of Hyogo, Kamigori, Hyogo 678-1297, Japan*

³*Brookhaven National Laboratory, Upton, NY 11937-5000, U. S. A.*

We performed the Te-nuclear magnetic resonance, the Mo-nuclear quadrupole resonance, and the AC susceptibility in the Weyl semimetal superconductor $1T\text{-MoTe}_2$ at pressures up to 2.17 GPa. From the temperature and pressure dependence of the AC susceptibility, the superconducting transition temperature T_c and the upper critical field H_{c2} were estimated. The results deviate from the Werthamer-Helfand-Hohenberg model but are well described by $H_{c2}(T) = H_{c2}(0)[1 - T/T_c]^\alpha$. The latter fit yields $H_{c2}(0) = 1.50$ T, $T_c = 3.81$ K, and $\alpha = 1.1$ at 2.17 GPa, suggesting that the superconductivity lies in a strong-coupling regime. Since the nuclear spin-lattice relaxation rate divided by temperature, $1/T_1T$, follows the Korringa relation at ambient pressure, the increase in $1/T_1T$ with pressure up to approximately 0.7 GPa indicates an increase in the density of states (DOS), $N(E_F)$. This trend mirrors the pressure dependence of T_c in the low-pressure region, consistent with the BCS mechanism. Above 0.7 GPa, however, $N(E_F)$ slightly decreases while T_c continues to rise, suggesting an additional pairing contribution beyond the conventional BCS picture. In the $1T'$ phase at 2.17 GPa, the absence of a coherence peak in $1/T_1T$ around T_c , accompanied by a two-step decrease just below T_c , was observed, which may be a signature of unconventional superconductivity.

1. Introduction

In condensed matter physics, the concept of topology has become a fundamental framework for understanding a wide range of quantum materials, including topological insulators and semimetals. Weyl semimetals, a class of topological materials, host the condensed-matter analog of relativistic Weyl fermions that arise from the linear dispersion relation near discrete Weyl nodes in momentum space. These Weyl fermions give rise to exotic physical properties such as surface Fermi arcs^{1,2)} and chiral anomaly.^{3,4)} Recently, the Weyl semimetals are

also of growing interest for the potential superconductivity hosting Majorana fermions. In this context, 1T-MoTe₂ is a promising candidate for a platform to investigate the relationship between the Weyl fermions and the superconductivity. 1T-MoTe₂ undergoes a structural phase transition from the high-temperature 1T' phase (monoclinic, space group $P2_1/m$) to the low-temperature T_d phase (orthorhombic, space group $Pmn2_1$) which is accompanied by the breaking of inversion symmetry and the emergence of a type-II Weyl semimetal state.⁵⁾ The structural phase transition occurs at a transition temperature $T_t = 250$ K under ambient pressure.^{6–11)} T_t decreases linearly with increasing pressure down to 50 ~ 100 K at 0.8 GPa.^{8,9)} Beyond the pressure region near 0.8 GPa where the two phases coexist, the 1T' phase becomes dominant at all temperatures above $P \sim 1$ GPa.^{9,10)}

Remarkably, superconductivity emerges in the Weyl semimetal phase of MoTe₂ with a transition temperature (T_c) of approximately 0.1 K at ambient pressure.⁶⁾ Because T_c is extremely low at ambient pressure, detailed investigation of the superconducting state is experimentally challenging. The application of pressure enhances T_c to about 4 K at 2 GPa.^{6–12)} This enhancement has motivated extensive studies on the possible realization of topological superconductivity. However, while the origin of the T_c enhancement remains unclear, the superconducting pairing symmetry is still under debate, with muon-spin rotation¹²⁾ and point-contact spectroscopy¹¹⁾ indicating possible s^{++} or s^{+-} states among several candidates.

From a microscopic perspective, it is desirable to employ experimental probes that can simultaneously access both the Weyl fermion states and the superconducting order. Nuclear magnetic resonance (NMR) is particularly suited for this purpose, as it can probe both the electronic states associated with superconductivity and those related to Weyl fermions.

The main objective of this study is to investigate low-energy density of states (DOS) near the Fermi level under pressure and to clarify how they influence the pressure-induced enhancement of T_c in 1T-MoTe₂. We measured the temperature and pressure dependence of the Knight shift (K) and the nuclear spin-lattice relaxation rate ($1/T_1$), which probe the static and dynamic spin susceptibilities, respectively, in both the 1T' and T_d phases, whose crystal structures are shown in Fig. 1 (a) and (b). The first-principles calculations of the DOS and the electric field gradient (EFG) were used to support the interpretation of the experimental results. The calculated EFG values also allowed us to estimate the expected NQR frequencies, facilitating the identification of the observed NQR signals. Section 3 outlines the experimental methods, and Section 4 presents and discusses the results, with conclusions summarized in Section 5.

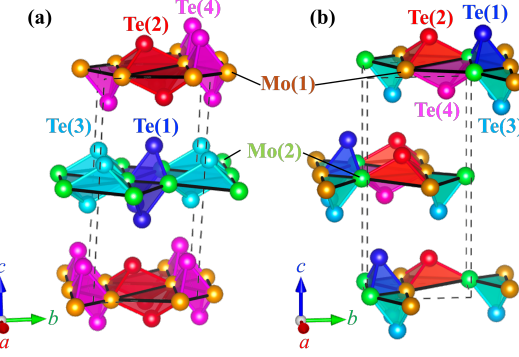


Fig. 1. (a) Crystal structure of the monoclinic 1T' phase. Each layer stacked along the c -axis contains only one type of Mo site, either Mo1 or Mo2. The cell parameters are $a = 3.469$, $b = 6.33$, $c = 13.86$ and $\beta = 93.92^\circ$.⁶⁾ (b) Crystal structure of the orthorhombic T_d -MoTe₂. Layers are stacked along the c -axis, and both Mo1 and Mo2 sites coexist within the same layer. The cell parameters are $a = 3.477$, $b = 6.335$, $c = 13.889$.⁶⁾ Both the 1T' and T_d phases form a layered structure stabilized by van der Waals forces between the layers, with Mo and Te atoms occupying two and four inequivalent sites, respectively. Within each layer, distorted pyramidal units are formed, with three Mo atoms at the base and a Te atom at the apex. These pyramids are arranged in a zigzag pattern along the a -axis and can be broadly classified into two distinct types: in the 1T' phase, each layer contains a single type of Mo site, whereas the T_d phase features two inequivalent Mo sites that alternate along the b -axis. Additionally, the layers in the 1T' phase alternately contain different Te atom pairs (Te(1, 2) or Te(3, 4)) along the c -axis, while the layers in the T_d phase all include four types of Te atoms. Despite these structural differences, a comparison of the local environments around the Te sites in both phases reveals only minor variations in the Mo-Te bond distances.

2. Calculation of density of states (DOS) and electric field gradient (EFG)

The DOS calculation in the T_d phase was performed for ambient pressure and 0.24 GPa by the Density Functional Theory (DFT) with the full-potential local-orbital code (FPLO) ver. 22, employing a local-orbital basis set.¹³⁾ To determine the atomic position parameters used in the DOS calculation, we performed crystal structural optimization based on the relaxation of atomic positions using LDA calculations. This calculation was carried out using the WIEN2k package,¹⁴⁾ with the lattice parameters adopted from those reported in Ref. ⁶⁾ For the calculation of the DOS using FPLO, we employed the LDA parametrized by Perdew and Wang¹⁵⁾ for the exchange-correlation potential, and the corresponding Brillouin zone was sampled using an $8 \times 8 \times 8$ k-mesh. The strong spin-orbit coupling was taken into account by performing full-relativistic calculations, wherein the Dirac Hamiltonian with a general potential is solved. The results of these calculations are presented in Fig. 2.

The Mo nuclear quadrupole frequency, ν_Q , can be obtained from the calculated EFG tensor at the Mo nuclear site. The EFG tensor elements, V_{ij} , are defined as the second

partial derivative of the electrostatic potential $V(\mathbf{r})$ at the position of the nucleus: $V_{ij} = (\partial_i \partial_j V(0) - \frac{1}{3} \delta_{ij} \Delta V(0))$, where $\delta_{i,j}$ is the Kronecker delta, with \mathbf{r} being the position vector originating from the nucleus. The calculated ν_Q and the asymmetric parameter of EFG, η , for the two inequivalent Mo sites, Mo(1) and Mo(2), in the T_d phase are tabulated in Table I. We note here that, according to the calculation, the distinct local environments of the two Mo sites in the T_d phase, as described in Fig. 1, do not lead to significant differences both in ν_Q and η .

Table I. Calculated EFG parameters, ν_Q and η , for the Mo(1) and Mo(2) site in the T_d phase. Expected two ^{97}Mo resonance frequencies, f_1 and f_2 , are also shown. See text for details.

Phase	$^{97}\nu_Q$ (MHz)	η	f_1 (MHz)	f_2 (MHz)
Mo(1)	5.84	0.87	9.42	10.52
Mo(2)	5.61	0.88	9.15	10.08

3. Experimental details

3.1 Sample Preparation: powder and single crystal.

The polycrystalline 1T- MoTe_2 was synthesized in a quartz ampoule sealed under vacuum, starting from a stoichiometric, intensively homogenized, mixture of element powders (Mo 99.95% Alfa Aesar and Te 99.999% Alfa Aesar) with the addition of 5 mg iodine as a reaction

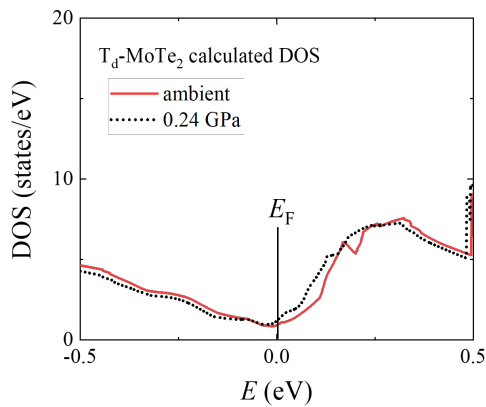


Fig. 2. Calculated total DOS as a function of energy in the T_d phase of MoTe_2 . The red and black curves are the calculated DOS corresponding to ambient and 0.24 GPa, respectively.

mediator. The reaction was carried out for 5 days at 600 °C and a further 5 days at 1000 °C. After homogenization of the reaction product obtained, this thermal treatment was repeated a second time. 1T-MoTe₂ single crystals were grown from Te flux.^{16,17)} Mo and Te raw elements were placed in an evacuated quartz tube in alumina crucibles in a ratio 1:25. The quartz tube was heated to 1000 °C for two hours, then cooled to 820 °C where excess Te flux was decanted in a centrifuge. Both samples synthesized in these ways were confirmed by x-ray diffraction to be in the 1T' phase at room temperature.

3.2 *NMR/NQR experiments.*

Mo NMR measurements would be the most direct method to investigate the magnetism and superconductivity of 1T-MoTe₂. However, due to the weak signal intensities, we restricted our ⁹⁷Mo NQR and ^{95,97}Mo NMR measurements to the spectrum of a powder sample at 4.2 K and ambient pressure. The NQR spectral measurements were performed by sweeping frequency, guided by the results of the DFT calculation (see Table I). We succeeded in observing resonances corresponding to the two transitions for a nuclear spin ⁹⁷I = 5/2, as described in Sec. 4.2. ^{95,97}NMR spectral measurements were carried out by sweeping external magnetic field. Both the ⁹⁵Mo and ⁹⁷Mo nuclei have I = 5/2. Obtained spectral data were analyzed using the gyromagnetic ratios ⁹⁵γ = 2.77 MHz/T and ⁹⁷γ = 2.83 MHz/T for the ⁹⁵Mo and ⁹⁷Mo, respectively.

¹²⁵Te NMR measurements (I = 1/2 and ¹²⁵γ = 13.45 MHz/T) were performed under ambient pressure and high pressures up to 2.17 GPa. The absence of nuclear quadrupole interactions simplifies the analyses of NMR spectrum and nuclear relaxation data. ¹²⁵Te-NMR spectra were obtained by fast Fourier transformation (FFT) of the spin-echo signal. A uniaxial rotation system was employed for measuring the angular dependence of the spectrum on the magnetic field. Nuclear spin-lattice relaxation rate (1/T₁) was measured at the same peak frequency using the inversion recovery method. The 1/T₁ values were extracted by fitting the recovery of the nuclear magnetization to the function $M(t) = M(\infty)(1 - c_0 \exp(-t/T_1))$, where $M(\infty)$ is the equilibrium nuclear magnetization, c_0 is a parameter indicating the degree of inversion ($c_0=2$ for complete inversion), and t is the time after the inversion pulse.

High-pressure measurements of ¹²⁵Te-NMR were carried out using a self-clamped BeCu/NiCrAl piston-cylinder cell. The 1T-MoTe₂ powder sample, NMR coil, a manganin wire gauge, and a lead manometer were placed inside a Teflon capsule filled with pressure-transmitting medium, as shown in Figs. 3(a), (b), and (c). A silicon-based organic liquid was used as the pressure medium. Pressure was determined by measuring the T_c of the lead. To

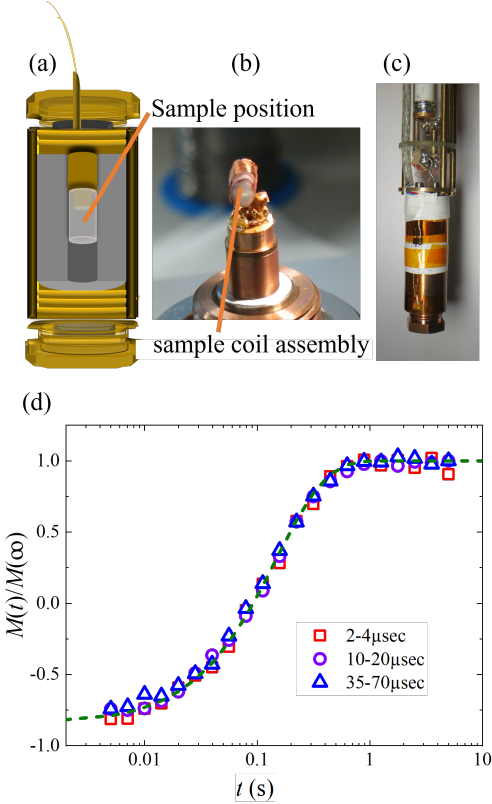


Fig. 3. (a) Schematic diagram of the self-clamped piston-cylinder cell. (b) NMR coil assembly. (c) NMR probe with the pressure cell and thermometers. (d) RF power dependence of nuclear magnetization recovery, $M(t)/M(\infty)$ vs t . The data were acquired at 4.2 K and 1.35 GPa, using an NMR measuring frequency of 6.235 MHz, and with the following sets of $\pi/2 - \pi$ pulse widths: 2 - 4 μ sec, 10 - 20 μ sec, and 35 - 70 μ sec. The dashed line shows the theoretical curve with $T_1=0.15$ s.

ensure the absence of RF heating during the NMR experiment inside the cell, we examined the RF power dependence of the spin-echo shape and the recovery of nuclear magnetization after saturation. This was done by varying the excitation RF pulse width from 2 μ sec to 35 μ sec while maintaining the pulse inversion condition. As shown in Fig. 3(d), the negligible difference in the recovery curves indicates the absence of RF heating under our experimental conditions.

4. Experimental results and discussions

4.1 AC-susceptibility measurements.

The macroscopic superconducting properties—particularly the upper critical field, H_{c2} —have been investigated using AC susceptibility measurements. It is known that the onset of superconductivity causes a significant change in the impedance of a tuned RF circuit.

Figure 4(a) shows a schematic diagram of a series RLC resonant circuit used for NMR

measurements. The total impedance Z_S of the circuit is expressed as $Z_S = R_S + iX_S$, where R_S represents the effective resistance accounting for energy losses related to the loaded and unloaded quality factors (Q_S and Q_0), as given by $R_S = G_1 \left(\frac{1}{2Q_S} - \frac{1}{2Q_0} \right)$. The reactance X_S describes the frequency-dependent deviation from its resonant frequency f_0 , which corresponds to the resonant frequency at 4.2 K, and is expressed as $X_S = G_2 \left(-\frac{f_S - f_0}{f} \right) + C$. Here, G_1 and G_2 are scaling factors determined by circuit parameters, f_S denotes the resonant frequency at each temperature and C represents an offset constant. In this setup, the imaginary part of the impedance is directly related to superconducting diamagnetism via shifts in the resonant frequency. This provides an effective method for detecting the onset of superconductivity using the same coil employed for NMR measurements.

As a representative example at 2.17 GPa, the fractional change in resonant frequency, $\Delta f/f_0 = (f_S - f_0)/f_0$, is plotted as a function of temperature under various applied magnetic fields in Fig. 4(b). The T_c were determined as the temperatures at which the resonant frequency dropped by 0.5% below the normal-state value for each field.

Simple BCS theory predicts that the Cooper pair breaking depends on the combined effects of Pauli paramagnetism and orbital diamagnetism. If we follow the Werthamer-Helfand-Hohenberg (WHH) theory in the weak-coupling regime,¹⁸⁾ the orbital-limiting upper critical field H_{c2} can be expressed as $H_{c2}(T) = H_{c2}(0) \left[1 - \left(\frac{T}{T_c} \right)^2 \right]$, where $H_{c2}(0) = -0.693 T_c \left(\frac{dH_{c2}}{dT} \right)_{T_c}$ and $\left(\frac{dH_{c2}}{dT} \right)_{T_c}$ is the initial slope of $H_{c2}(T)$ at T_c . Dashed lines in Fig. 4(c) show these fits for 2.17, 1.35, and 0.68 GPa. Although we obtained zero-temperature upper critical fields of $H_{c2}(0) = 0.75$ T, 0.42 T, and 0.096 T for 2.17 GPa, 1.35 GPa, and 0.68 GPa, respectively, a clear deviation from the experimental data is observed at lower temperatures. To address this discrepancy, we used the phenomenological expression $H_{c2}(T) = H_{c2}(0) \left[1 - \left(\frac{T}{T_c} \right) \right]^\alpha$ to fit the data.¹⁹⁾ We obtained $H_{c2}(0)$, T_c , and α for 2.17 GPa, 1.35 GPa, and 0.68 GPa, which are summarized in Table II.

The increase of $H_{c2}(0)$ with pressure and the fact that α is greater than one suggest that 1T-MoTe₂ belongs to a strong-coupling regime under high pressures.

Table II. Pressure dependence of T_c , $H_{c2}(0)$, and α obtained from fitting.

Pressure (GPa)	T_c (K)	$H_{c2}(0)$ (T)	α
0.68	1.94	1.14	1.8
1.35	2.97	1.21	1.4
2.17	3.81	1.50	1.1

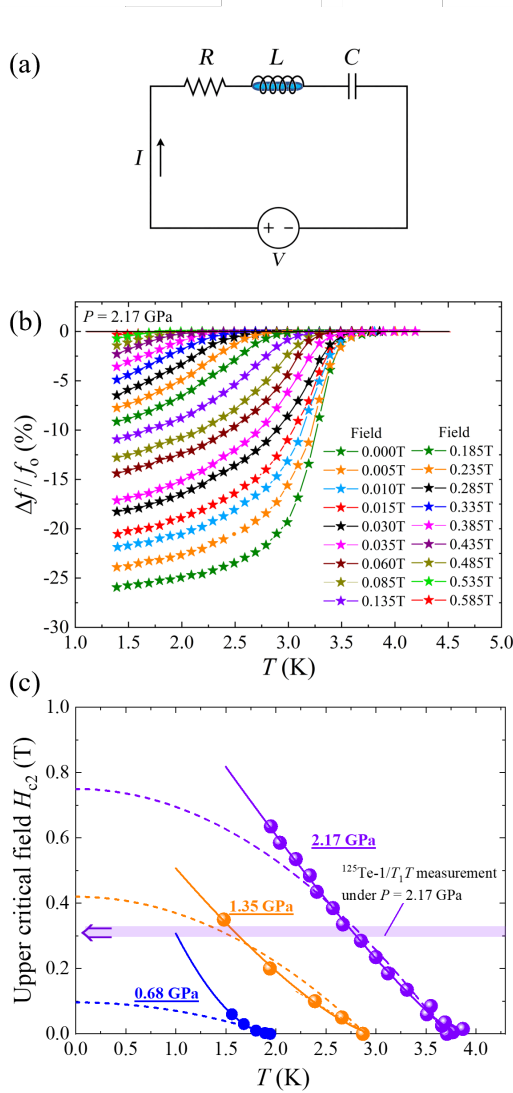


Fig. 4. (a) Equivalent circuit of NMR and ac susceptibility measurements. (b) Imaginary part of impedance of tune circuit measured by frequency cage, $(\Delta f)/f_0 = (f_s - f_0)/f_0$ as a function of temperature under 2.17 GPa. (c) Temperature dependence of upper critical field, H_{c2} , under 2.17 GPa (violet), 1.35 GPa (orange) and 0.68 GPa. The dashed lines are expected $H_{c2}(T)$ from WHH model, and solid lines are fit to $H_{c2}(T) = H_{c2}(0) \times [1 - T/T_c]^\alpha$ (see main text).

4.2 Mo NQR and NMR at ambient pressure

The ^{97}Mo NQR spectrum at 4.2 K in the T_d phase is shown in Fig. 5(a), which was successfully identified with the help of the DFT calculation (see Table I). The observed peak frequencies f_1 and f_2 are assigned to the transitions between the nuclear quadrupolar split energy levels of $3/2 \leftrightarrow 1/2$ and $5/2 \leftrightarrow 3/2$, respectively.

From these values, ν_Q and η are determined to be $^{97}\nu_Q = 0.54$ and $\eta = 0.73$, respectively.

For f_1 and f_2 , the maximum discrepancy between the prediction by the DFT calculation and the experimental value is approximately 16%, demonstrating that highly accurate DFT calculations prove to be a powerful tool in the detection of unknown NQR signals. It should be noted that because of the small differences in ν_Q and η between the Mo(1) and Mo(2) sites, as suggested by the DFT calculation, the site differentiation was not observed in the present NQR spectra.

Field-swept $^{95/97}\text{Mo}$ -NMR powder spectra obtained at 4.2 K are shown in Fig. 5(b). The observed spectrum is composed of ^{95}Mo and ^{97}Mo NMR signals with a typical powder pattern. Due to the one order of magnitude larger quadrupole moment of ^{97}Mo , we expect to observe only a second-order powder spectrum for the central transition. Using the same EFG parameters obtained from the NQR spectra and taking into account the natural abundance ratio of ^{95}Mo and ^{97}Mo , we simulated the NMR spectrum by convoluting ^{95}Mo and ^{97}Mo components, as shown in Fig. 5(b). Here, the Mo(1) and Mo(2) sites were treated as being indistinguishable. The consistency between the simulated and observed spectra, along with the agreement between the theoretically predicted and experimental NQR spectra, clearly demonstrates the high reliability of the DFT calculation, thereby enabling subsequent discussion based on the DOS.

4.3 Te NMR under pressure: Spectra and Knight Shift

As mentioned in Sec.3.2, ^{125}Te NMR is a highly suitable tool for investigating the microscopic static and dynamic properties of 1T-MoTe₂. However, data analysis can be challenging due to the frequent presence of unknown transferred hyperfine interactions at the Te sites. Despite this drawback, the nuclear spin $I = 1/2$ and relatively large gyromagnetic ratio ($\gamma_n = 13.45$ MHz/T) provide significant advantages: they enable signal detection under high-pressure and high-temperature conditions and facilitate data analysis without the complications arising from nuclear quadrupole interactions. As an example, the ^{125}Te NMR spectrum is shown in Fig. 6.

In general, these data can be obtained either by performing an FFT of the spin-echo signal at a constant magnetic field or by using the frequency (or field) sweep method. The former is more suitable for relatively narrow lines, while the latter is better suited for broad lines. We first measured the NMR spectrum at 5 K using both methods and compared the results. As shown in Fig. 6, the spectra from both methods matched perfectly. Therefore, we primarily used the FFT method to acquire data for temperature and pressure dependence studies. It should be noted that the spectrum shown in Fig. 6 is a typical powder pattern with uniaxial

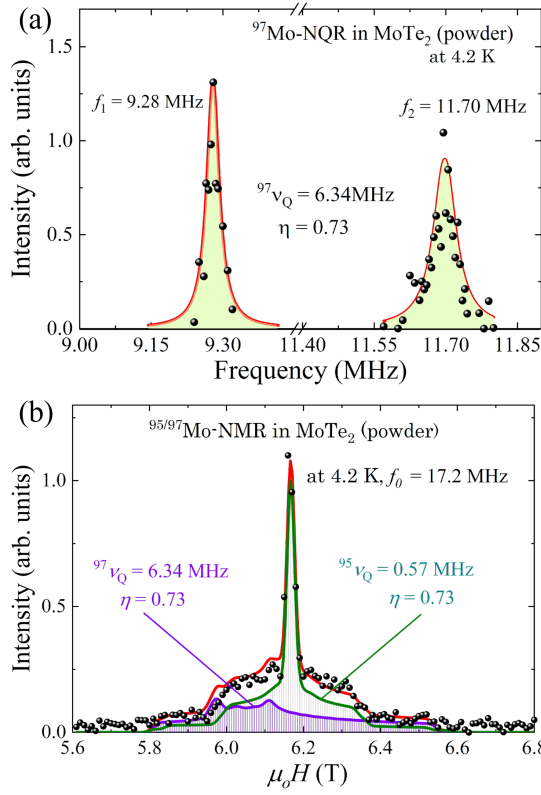


Fig. 5. (a) Frequency-swept ^{97}Mo NQR spectrum measured at 4.2 K. From the two observed resonances at $f_1 = 9.28$ MHz and $f_2 = 11.70$ MHz, we obtained $^{97}\nu_Q = 6.34$ MHz and $\eta = 0.73$. Field-swept ^{95}Mo and ^{97}Mo NMR spectra measured using a measuring frequency of 17.2 MHz at 4.2 K. The green and purple lines are simulated spectra using $^{95}\nu_Q = 0.57$ MHz for ^{95}Mo and $^{97}\nu_Q = 6.34$ MHz for ^{97}Mo , with $\eta = 0.73$ being common to both. Here, $^{95}\nu_Q$ was calculated from the result of $^{97}\nu_Q = 6.34$ MHz and the ratio of nuclear quadrupole moment $^{95}Q/^{97}Q = 0.086$. The red line is the sum of them.

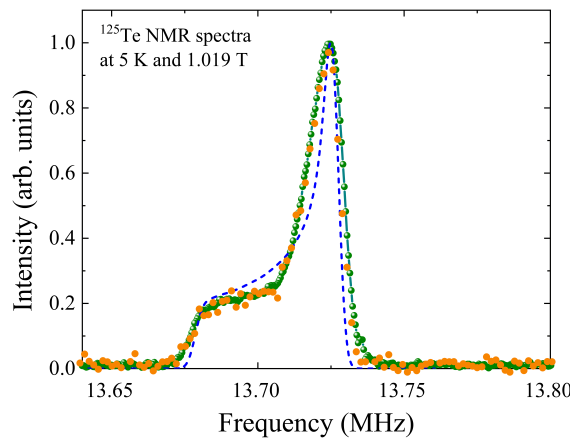


Fig. 6. A typical ^{125}Te -NMR spectrum at 5 K and 1.019 T is shown. The frequency spectrum was obtained by performing an FFT on the spin echo signal (green dots connected by a line) and is compared with data acquired using the field sweep method (orange circles). The dashed line represents a simulated axial symmetry powder pattern with $K_{\text{iso}} = 0.02\%$ and $K_{\text{ax}} = -0.05\%$.

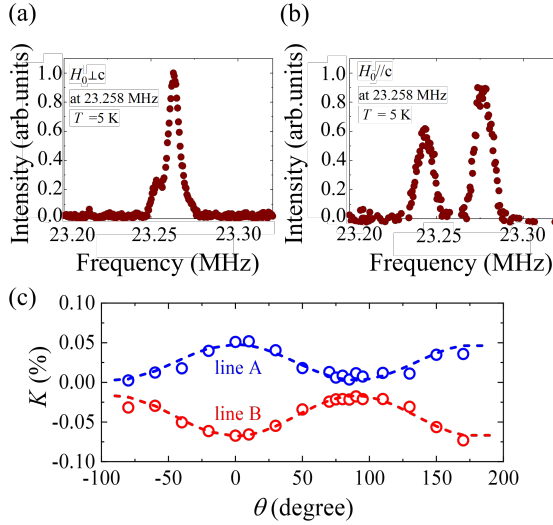


Fig. 7. Angular dependence of ^{125}Te NMR spectra at 5 K and 23.258 MHz: (a) Applied magnetic field parallel to the c -axis A; (b) Applied field perpendicular to the c -axis B. (c) Angular dependence of the K for two distinct groups of Te sites. The dashed lines represent the function $K(\theta) = K_{\text{iso}} + K_{\text{ax}}(3 \cos^2 \theta - 1)$. These results are consistent with the 90° rotational symmetry of the orthorhombic crystal structure.

symmetry. Under this assumption, we successfully obtained the best simulated spectrum with $K_{\text{iso}} = 0.02\%$ and $K_{\text{ax}} = -0.05\%$, as shown by the dashed line in Fig. 6.

We also successfully observed ^{125}Te NMR spectra in a single crystal. The θ -dependence of the spectrum, where θ is the angle between the crystal c -axis and the magnetic field H_0 , was measured using a uniaxial rotation system. As shown in Fig. 7, two distinct groups of resonance lines (A and B) were observed, and both lines exhibit two-fold rotational symmetry with respect to θ , reflecting the orthorhombic structure of the T_d phase. The two observed lines likely originate from two pairs of the four inequivalent Te sites, i.e. (Te(1), Te(3)) and (Te(2), Te(4)), that have a similar local environment surrounded by the Mo atoms. Thus, although the T_d phase lacks inversion symmetry along the c -axis, no phenomena stemming from this unique structure were observed in the present measurements. The θ -dependence of the spectrum reveals that the lines A and B become proximate to each other, when $H_0 \perp c$. This behavior is consistent with the assumption of uniaxial symmetry used in the powder spectrum fit (see Fig. 6). The θ dependence of the Knight shift, $K(\theta)$, can be fitted by a typical expression for an axially symmetric system: $K(\theta) = K_{\text{iso}} + K_{\text{ax}}(3 \cos^2 \theta - 1)$, yielding $K_{\text{iso}} = 0.018\%$ and $K_{\text{iso}} = 0.015\%$ for line A; and $K_{\text{iso}} = -0.034\%$ and $K_{\text{ax}} = -0.017\%$ for line B. However, due to the limitation of our uniaxial rotation system, we have not obtained the comprehensive line profile of the single-crystal necessary to examine the overall consistency

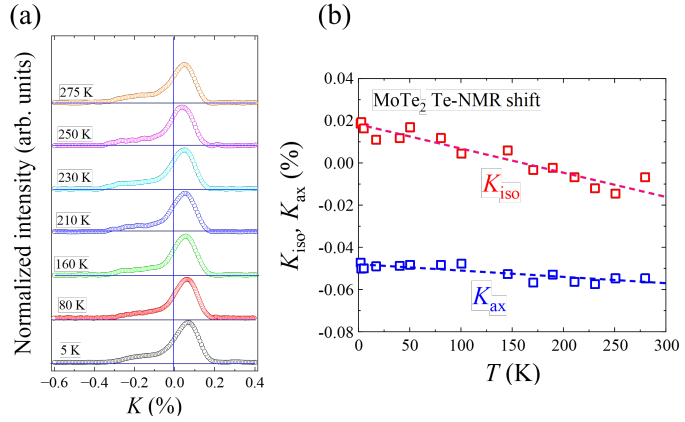


Fig. 8. (a) Temperature dependence of FFT spectrum measured at 1.0186 T. (b) Temperature dependence of K_{iso} and K_{ax} under ambient pressure.

with the powder pattern. Therefore, we will focus our discussion on the powder data in the following sections, and our future efforts will involve further detailed spectral measurements of the field angular dependence.

The temperature dependence of ^{125}Te NMR powder spectrum at ambient pressure and its pressure dependence of at 5 K were measured. The results are shown in Figs. 8(a) and 9(a), respectively. Also extracted K_{iso} and K_{ax} are displayed in Figs. 8(b) and 9(b), respectively. K_{ax} shows little dependence on either temperature or pressure. In contrast, the K_{iso} gradually decreases with increasing temperature, suggesting the temperature-dependent magnetic susceptibility. Furthermore, K_{ax} exhibits a distinctive pressure dependence: it initially increases rapidly up to about 0.7 GPa, and since this behavior is consistent with the pressure dependence of T_c , these behaviors are likely related to the DOS at the Fermi level. Upon further pressure increase, K_{iso} begins to decrease, and its overall pressure dependence closely resembles that of the nuclear spin-lattice relaxation rate divided by temperature, $1/T_1T$, which will be discussed in Section 4.4.1.

It should also be noted that 1T- MoTe_2 undergoes a first-order phase transition from the high-temperature monoclinic 1T' phase to the low-temperature orthorhombic T_d phase at 250 K.^{6-10, 12)} The T_d phase reverts to the 1T' phase under increasing pressure, with the 1T' phase being stabilized above 1 GPa at all temperatures.^{9, 10)} However, the Te-NMR spectra do not exhibit any signs of this phase transition, nor do they show any site distinction. This indicates that the transferred hyperfine interaction at the Te sites is insensitive to changes in crystal symmetry.

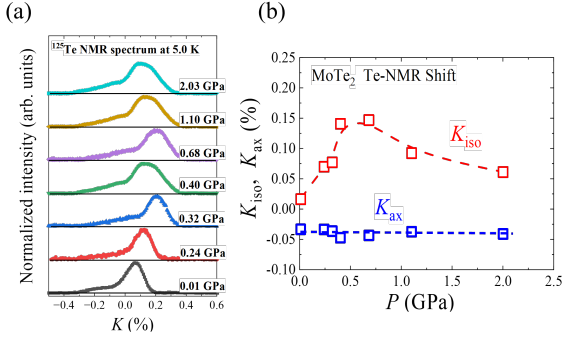


Fig. 9. (a) Pressure dependence of FFT spectrum. (b) Pressure dependence of K_{iso} and K_{ax} measured at 5 K.

4.4 *Te NMR under pressure: Nuclear spin-lattice relaxation*

4.4.1 *Normal state*

We measured the ^{125}Te NMR T_1 at the main peak position of the spectrum at pressures up to 2.17 GPa. When the relaxation process is magnetic, which is the case for ^{125}Te with $I = 1/2$, $1/T_1T$ can be generally expressed by the dynamical susceptibility $\chi(\mathbf{q}, \omega)$, where \mathbf{q} is the wave vector and ω is the frequency, as shown in the following equation:^{20,21)}

$$\left(\frac{1}{T_1T} \right) = \frac{2\gamma_N^2 k_B}{g^2 \mu_B^2} \sum_{\mathbf{q}} A_{\mathbf{q}}^2 \frac{\chi''(\mathbf{q}, \omega)}{\omega_N}. \quad (1)$$

Here, γ_N is the gyromagnetic ratio, k_B is a Boltzmann constant, g is called the g -factor, μ_B is a Bohr magneton, $\chi''(\mathbf{q}, \omega)$ is the transverse component of the imaginary part of dynamical susceptibility, ω_N is the NMR frequency, $A_{\mathbf{q}}$ is the \mathbf{q} -dependent hyperfine coupling constant. In MoTe₂, the hyperfine field at the Te sites originates from both the Fermi contact interaction with conduction electrons and the transferred hyperfine interaction with neighboring Mo moments through d - p mixing. Because our experimental observations provide clear evidence that the former mechanism dominates the relaxation process at least at low temperatures we analyze the experimental results using an electron-band framework within the random phase approximation (RPA) as follows:

$$\left(\frac{1}{T_1T} \right) \propto \frac{A_{\text{hf}}^2}{T} \int f(E)[1 - f(E)]\{N(E)\}^2 dE, \quad (2)$$

where A_{hf} is the \mathbf{q} -averaged hyperfine coupling constant, $N(E)$ is the energy-dependent DOS near the Fermi level, and $f(E)$ is the Fermi distribution function.

The temperature dependence of the $1/T_1T$ is shown in Fig. 10. The data exhibit a Korringa-type behavior, characterized by temperature independence of $1/T_1T$ below approx-

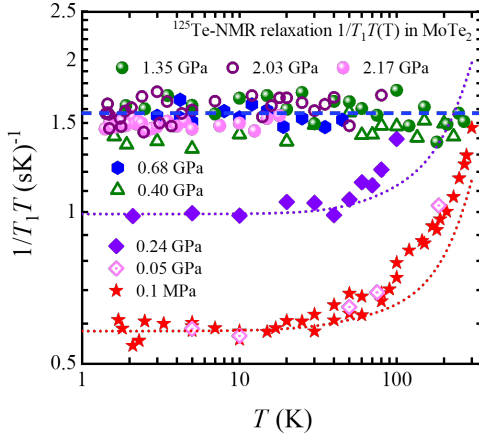


Fig. 10. Temperature dependence of $1/T_T$ measured at the Te site in the T_d phase up to 2.17 GPa. The red and violet dashed lines represent calculated $1/T_T(T)$ at ambient pressure and 0.24 GPa, respectively, based on the DOS shown in Fig. 2.

imately 30 K. In contrast, $1/T_1T$ increases rapidly above $T \sim 30$ K. According to our DFT calculation, the energy dependence of the DOS forms a V-shaped DOS around E_F , as shown in Fig. 2. This plausibly leads to the increase in $1/T_1T$ with increasing temperature due to the contribution of the DOS at energy levels away from E_F . Another notable feature is the strong pressure dependence of the Korringa term at relatively low pressures: the temperature independent $1/T_1T$ increases (from 0.6) to $1.5(\text{sec} \cdot \text{K})^{-1}$ with increasing the pressure to approximately 0.7 GPa.

Indeed, these trends are reproduced by computing Eq. (2) using the DOS at ambient pressure and 0.24 GPa in the T_d phase shown in Fig. 2. Here, since A_{hf} is unknown, the calculated values of $1/T_1T$ are normalized to the experimental value obtained at low temperature. The calculated $1/T_1T$ at ambient pressure, shown by the red dotted curve in Fig. 10, increases at high temperatures, consistent with the experimental results, despite the calculated increase being slightly shifted toward higher temperatures compared to the measured temperature dependence. Moreover the constant $1/T_1T$ value at low temperatures increases at 0.24 GPa, while the similar temperature dependence is maintained, as shown by the violet dotted curves in Fig. 10. These trends are in overall good agreement with the experimental results.

Next, we discuss the pressure dependence of the low-temperature $1/T_1T$ and T_c based on the simplified expression for the Korringa rate and the BCS expression for T_c . We here adopt the equation of the Korringa relation for weakly interacting electron systems^{22,23)} described

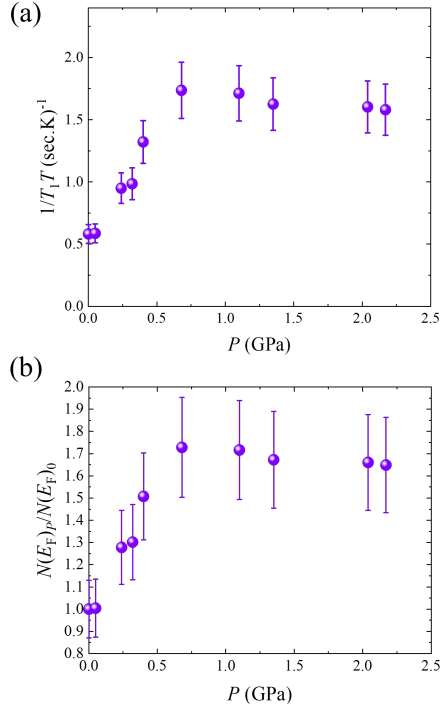


Fig. 11. (a) Pressure dependence of the low-temperature $1/T_1T$. Pressure dependence of normalized DOS $N_s(E_F)_p/N_s(E_F)_0$ estimated using the Korringa relation described by Eq. (3).

next:

$$\left(\frac{1}{T_1T}\right)_s = \frac{4\pi k_B}{\hbar}(\gamma_n \hbar H_{\text{hf}}^s)^2 (N(E_F))^2, \quad (3)$$

where $\left(\frac{1}{T_1T}\right)_s$ represents the spin component of $1/T_1T$ and H_{hf}^s is the hyperfine field per spin at the nuclear site. The pressure dependences of the constant $1/T_1T$ at low temperature and $N(E_F)_p/N(E_F)_0$ estimated from the relation in Eq. 3 are shown in Fig. 11(b), where $N(E_F)_p$ is normalized to unity at ambient pressure. It should be noted that the DOS increases almost linearly with pressure up to about 0.7 GPa, followed by a slightly decrease at higher pressures. On the other hand, T_c is described by the following well-known BCS formula²⁴⁾ :

$$T_c = 1.13\Theta_D \exp\left[-\frac{1}{V_0 N(E_F)}\right], \quad (4)$$

where Θ_D is the Debye temperature and V_0 is the interaction strength.

If we assume no significant change of Θ_D and V_0 with pressure, we can simply compare the pressure dependences of T_c and $N(E_F)_p/N(E_F)_0$ (shown in Fig. 11) via the relation $T_c(P) = T_c(0) \exp\left[-a \left\{\left(\frac{N(E_F)_p}{N(E_F)_0}\right)^{-1} - 1\right\}\right]$, where a is a constant. Such plots are shown in Fig. 12. We can immediately observe that below ~ 0.7 GPa (in the T_d orthorhombic phase),

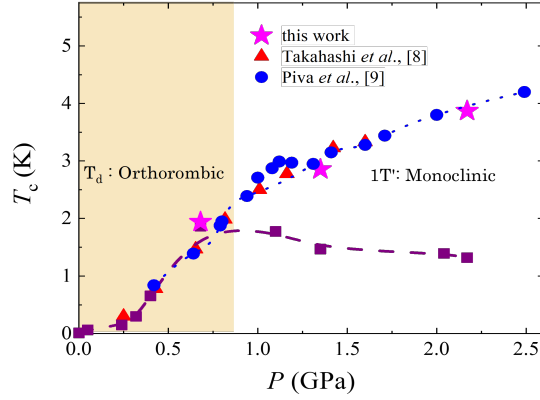


Fig. 12. Comparison of the pressure dependence of T_c (red and blur circles) from Refs. 8 and 9, respectively, and that expected from the BCS relation between T_c and the DOS (Fig. 11). See text for details. The latter is normalized to match the measured T_c at ambient pressure.

the pressure dependence of T_c determined experimentally as shown in Fig. 12 is in general agreement with that of $N(E_F)$. However, above ~ 0.7 GPa, the experimental T_c exhibits a distinctly different behavior from what is expected from the pressure dependence of $N(E_F)$ shown in Fig. 11(b). This suggests the presence of an additional pairing mechanism beyond the conventional phonon-mediated BCS framework possibly involving spin fluctuations that are enhanced T_c under pressure.

4.4.2 Superconducting state

In order to gain deeper insights into the mechanism of superconductivity in 1T-MoTe₂, it is essential to clarify the order parameter below T_c . Typically, this will be achieved by studying the temperature and pressure dependence of the nuclear relaxation time, T_1 . Unfortunately, the current NMR equipment is unable to access the low temperatures and high pressures required for such measurements. Despite this limitation, we attempted to measure the temperature dependence of T_1 at our highest pressure (2.17 GPa), using the lowest NMR frequency (4.34 MHz, corresponding to an applied field of 0.314 T) and down to the lowest temperature of 1.45 K. We present the results in Fig. 13, where the measurements were carried out after three different cooling procedures. Initially, we measured $1/T_1T$ under zero-field-cool and field-cool conditions at 6.29 MHz (0.464 T). As shown by blue and green squares, no evidence for the onset of superconductivity was observed. However, when we reduced the frequency to 4.34 MHz corresponding to 0.31 T, a signature of the onset of superconductivity was observed (see the red dotted circles in Fig. 13). As indicated by Fig. 3 (c), the AC-susceptibility measurement of the present sample predict T_c should be around

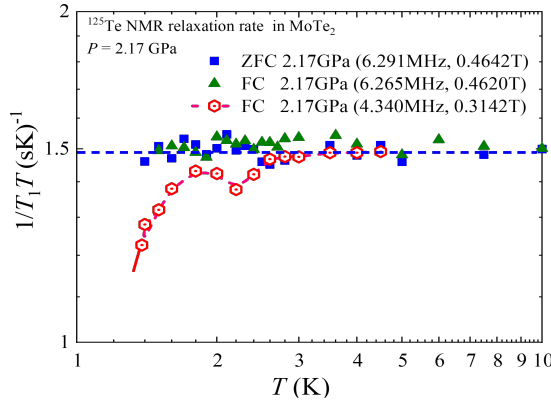


Fig. 13. Temperature dependence $1/T_1T$ measured by ^{125}Te NMR after three different cooling procedures. Blue and green squares represent the data measured at 6.291 MHz after zero-field cooling (ZFC) and at 6.265 MHz after field cooling (FC), respectively. Dotted red circles represent the data measured at 4.340 MHz after field cooling.

2.7 K, which just corresponds to the point where the reduction of $1/T_1T$ begins with cooling. Although we need more data across different fields, the following points can be argued: 1) There is no increase in $1/T_1T$ just above T_c (the so called coherence peak) characteristic to the simple phonon mediated s -wave superconductivity, 2) The temperature dependence of $1/T_1T$ exhibits a characteristic two-step decrease which cannot be expressed by the single superconducting gap, indicating that 1T-MoTe₂ has a multi-gap superconducting state. This has been argued by μ SR measurements at pressure between 0.45 GPa and 1.3 GPa.¹²⁾ The present data does not give us a conclusive result for the superconductivity associated with the topologically trivial 1T'-phase of MoTe₂. Nevertheless, there exist several important hints which motivate further experiments to explore broader pressure and temperature ranges to refine the data and gain more conclusive evidence.

5. Concluding remarks

We have employed AC-susceptibility and microscopic techniques specifically Nuclear Magnetic Resonance (NMR) and Nuclear Quadrupole Resonance (NQR) to investigate the fundamental properties of the pressure-induced topological superconductivity candidate 1T-MoTe₂. Our study includes detailed measurements of the pressure dependence of superconducting transition temperature T_c and upper critical field (H_{c2}), and the temperature dependence of NMR/NQR line shapes, Knight shift, and nuclear spin-lattice relaxation rate ($1/T_1$).

- The T_c was determined from the resonance frequency shift of the NMR tuning circuit and its magnetic field and pressure dependences were investigated. By fitting the field

dependence of T_c using the phenomenological relation $H_{c2}(T) = H_{c2}(0) \times [1 - (T/T_c)]^\alpha$, we extracted the values of $H_{c2}(0)$, T_c , and α at pressures of 2.17 GPa, 1.35 GPa, and 0.68 GPa. The analysis reveals an increase in $H_{c2}(0)$ and a decrease in α with increasing pressure, suggesting that 1T-MoTe₂ enters a strong-coupling superconducting regime under high pressure.

- The structural phase transition from T_d to 1T' phase was not detected through either the temperature or pressure dependence of the ¹²⁵Te NMR line profiles. This indicates that the transferred hyperfine interactions are largely insensitive to changes in crystal symmetry and slight variations in lattice parameters.
- The temperature and pressure dependence of $1/T_1T$ is consistent with the prediction from the DFT calculations. The relative DOS, estimated from the Korringa relation, was found to increase with pressure up to approximately 0.7 GPa. This mirrors the pressure dependence of the T_c , which can be explained by the conventional BCS theory. In contrast, the DOS gradually decreases with increasing pressure above 0.7 GPa, while T_c continues to increase. This discrepancy suggests that additional contributions – likely of magnetic origin – play a significant role in the emergence of superconductivity under higher pressure.
- In the superconducting state, a multi-gap superconducting behavior was observed at 2.17 GPa and 3 K, where the system remains in the topologically trivial 1T' phase.

The present study on 1T-MoTe₂ highlights that many open questions remain concerning the relationship between electronic topology and superconductivity. In particular, NMR data especially the temperature dependence of $1/T_1T$ in the superconducting state is highly anticipated to provide further insight. A detailed investigation of the pressure and temperature dependence of the superconducting order parameter is essential for exploring the potential realization of topological superconductivity. We believe that the current work offers valuable progress and sheds light on this promising direction.

Acknowledgment

We acknowledge fruitful discussions with Mario Moda Piva, Deepa Kashinathan and Michael Nicklas. We would like to thank Vicky Hasse for support during the synthesis. Work at Brookhaven National Laboratory was supported by the U.S. Department of Energy, Office of Science, Office of Basic Energy Sciences under Contract No. DE-SC0012704 (materials synthesis). T. F. appreciate the financial support from JSPS KAKENHI Grants (No. 15K21732).

Present address

★ Department of Physics, Indian Institute of Technology Palakkad, Kerala 678623, India

† Center for Correlated Matter and School of Physics, Zhejiang University, Hangzhou 310058, China

* Shanghai Key Laboratory of Material Frontiers Research in Extreme Environments (MFree), Shanghai Advanced Research in Physical Sciences (SHARPS), Shanghai 201203, China

References

- 1) S.-Y. Xu, I. Belopolski, N. Alidoust, M. Neupane, G. Bian, C. Zhang, R. Sankar, G. Chang, Z. Yuan, C.-C. Lee, et al.: *Science* **349** (2015) 613.
- 2) B. Lv, H. Weng, B. Fu, X. P. Wang, H. Miao, J. Ma, P. Richard, X. Huang, L. Zhao, G. Chen, et al.: *Physical Review X* **5** (2015) 031013.
- 3) X. Huang, L. Zhao, Y. Long, P. Wang, D. Chen, Z. Yang, H. Liang, M. Xue, H. Weng, Z. Fang, et al.: *Physical Review X* **5** (2015) 031023.
- 4) C.-L. Zhang, S.-Y. Xu, I. Belopolski, Z. Yuan, Z. Lin, B. Tong, G. Bian, N. Alidoust, C.-C. Lee, S.-M. Huang, et al.: *Nature communications* **7** (2016) 1.
- 5) R. Sankar, G. Narsinga Rao, I. P. Muthuselvam, C. Butler, N. Kumar, G. Senthil Murgan, C. Shekhar, T.-R. Chang, C.-Y. Wen, C.-W. Chen, et al.: *Chemistry of Materials* **29** (2017) 699.
- 6) Y. Qi, P. G. Naumov, M. N. Ali, C. R. Rajamathi, W. Schnelle, O. Barkalov, M. Hanfland, S. C. Wu, C. Shekhar, Y. Sun, V. Süß, M. Schmidt, U. Schwarz, E. Pippel, P. Werner, R. Hillebrand, T. Förster, E. Kampert, S. Parkin, R. J. Cava, C. Felser, B. Yan, and S. A. Medvedev: *Nat. Commun.* **7** (2016) 11038.
- 7) Y. J. Hu, Y. T. Chan, K. T. Lai, K. O. Ho, X. Guo, H.-P. Sun, K. Y. Yip, D. H. L. Ng, H.-Z. Lu, and S. K. Goh: *Phys. Rev. Mater.* **3** (2019) 034201.
- 8) H. Takahashi, T. Akiba, K. Imura, T. Shiino, K. Deguchi, N. K. Sato, H. Sakai, M. S. Bahramy, and S. Ishiwata: *Phys. Rev. B* **95** (2017) 100501.
- 9) M. M. Piva, L. O. Kutelak, R. Borth, Y. Liu, C. Petrovic, R. D. dos Reis, and M. Nicklas: *Phys. Rev. Mater.* **7** (2023) L111801.
- 10) C. Heikes, I.-L. Liu, T. Metz, C. Eckberg, P. Neves, Y. Wu, L. Hung, P. Piccoli, H. Cao, J. Leao, J. Paglione, T. Yildirim, N. P. Butch, and W. Ratcliff: *Phys. Rev. Mater.* **2** (2018) 074202.
- 11) D. Zhang, Z. Xu, T. Le, C. Chen, G. Ye, F. Shi, S. Luo, Y. Shi, and X. Lu: *Phys. Rev. B* **109** (2024) 144506.
- 12) Z. Guguchia, F. von Rohr, Z. Shermadini, A. T. Lee, S. Banerjee, A. R. Wieteska, C. A. Marianetti, B. A. Frandsen, H. Luetkens, Z. Gong, S. C. Cheung, C. Baines, A. Shengelaya, G. Taniashvili, A. N. Pasupathy, E. Morenzoni, S. J. L. Billinge, A. Amato, R. J. Cava, R. Khasanov, and Y. J. Uemura: *Nat. Commun.* **8** (2017) 1082.
- 13) K. Koepernik and H. Eschrig: *Phys. Rev. B* **59** (1999) 1743.

- 14) F. Tran and P. Blaha: *Phys. Rev. Lett.* **102** (2009) 226401.
- 15) J. P. Perdew and Y. Wang: *Phys. Rev. B* **45** (1992) 13244.
- 16) Z. Wang, D. Gresch, A. A. Soluyanov, W. Xie, S. Kushwaha, X. Dai, M. Troyer, R. J. Cava, and B. A. Bernevig: *Phys. Rev. Lett.* **117** (2016) 056805.
- 17) J. Yang, J. Colen, J. Liu, M. C. Nguyen, G.-W. Chern, and D. Louca: *Sci. Adv.* **3** (2017) eaao4949.
- 18) N. R. Werthamer, E. Helfand, and P. C. Hohenberg: *Phys. Rev.* **147** (1966) 295.
- 19) K.-H. Müller, G. Fuchs, A. Handstein, K. Nenkov, V. N. Narozhnyi, and D. Eckert: *J. Alloys Compd.* **322** (2001) L10.
- 20) H. Narath and H. Weaver: *Phys. Rev.* **175** (1968) 373.
- 21) T. Moriya: *J. Phys. Soc. Jpn.* **18** (1963) 516.
- 22) C. P. Slichter: (Springer, New York, 1990) 3rd ed.
- 23) J. Korringa: *Physica* **16** (1950) 601.
- 24) J. Bardeen, L. N. Cooper, and J. R. Schrieffer: *Phys. Rev.* **108** (1957) 1175.